Assessing the accuracy of quantum dynamics performed in the time-dependent basis representation

Sophya Garashchuk*,† and Frank Großmann‡

†*Department of Chemistry & Biochemistry, University of South Carolina, Columbia, South Carolina 29208, United States*

‡*Institute for Theoretical Physics, Technische Universität Dresden, 01062 Dresden, Germany*

E-mail: garashchuk@sc.edu

Abstract

A full quantum-mechanical (QM) description of large amplitude nuclear motion, associated with chemical reactions or isomerization of high-dimensional molecular systems, is inherently challenging due to the exponential scaling of the QM complexity with system size. To ameliorate the scaling bottleneck in studies of realistic systems, typically modeled in configuration space, the nuclear wavefunctions are represented in terms of time-dependent basis functions. Such bases are expected to give an accurate description with a modest number of basis functions employed, by adapting them to the wavefunction solving the time-dependent Schrödinger equation. It is not, however, straightforward to estimate the accuracy of the resulting solution: in QM the energy conservation – a convenient such measure for a classical trajectory evolving in a time-independent potential – is not a sufficient criterion of the dynamics' accuracy. In this

work, we argue that the expectation value of the Hamiltonian's 'variance', quantifying the basis completeness, is a suitable practical measure of the quantum dynamics' accuracy. Illustrations are given for several chemistry-relevant test systems, modeled employing time-independent as well as time-dependent bases, including the Coupled and Variational Coherent States methods, and the Quantum-trajectory guided Adaptable Gaussians (QTAG) as the latter basis type. A novel semi-local definition of the QTAG basis time-evolution for placing the basis functions 'in the right place at the right time' is also presented.

1 Introduction

In order to cope with the exponential formal scaling of the complexity of quantum mechanics,[1] the nuclear wavefunctions of high-dimensional, i.e. beyond five-six degrees of freedom (DOFs), molecular systems undergoing large amplitude motion are often represented in terms of the time-dependent basis functions in configuration space. Gaussian basis functions (GBFs) are a particularly popular choice, because from the conceptual point of view a single complex Gaussian wavefunction, whose center moves classically, solves the time-dependent Schrödinger equation in a quadratic, possibly time-dependent, potential, and from the practical point of view localization of the GBFs in coordinate space is advantageous for on-the-fly evaluation of the potential energy and its gradients driving the wavefunction dynamics. Using a few examples most relevant to this work, the GBFs are employed in such approaches as (i) the Gaussian Multidimensional Time-Dependent Hartree and variational multiconfiguration Gaussian methods,[2,3] the Coupled Coherent States (CCS),[4,5] the Variational Coherent States (VCS),[6] the Quantum Trajectory-guided Adaptable Gaussian (QTAG) method,[7,8] (ii) Matching Pursuit[9] and Basis Expansions Leaping[10] and (iii) the basis generation from short-term trajectory dynamics.[11,12] Overviews of GBF methods are available in Refs.,[5,13–15] with the last reference devoted to the Davydov ansätze, that use GBF for the description of the bosonic part of the Hilbert space of a composite system. All of these methods are developed

primarily for multidimensional nuclear dynamics, characterized by a few 'active' modes coupled to multiple 'spectator' modes, such as the proton transfer in a water-hydronium system.

To update the basis parameters during the wavefunction dynamics, the GBF methods invoke (i) the trajectory framework evolving in time according to a set of equations of motion (EOMs), (ii) wavefunction reexpansions in a new GBF basis, or (iii) the combination of (i) and (ii), i.e. the EOMs guide the construction of new basis sets, but do not unambiguously define them. In all cases the GBFs are adapted or generated to ensure the accuracy of the time-dependent wavefunction in a small basis. Within the trajectory framework, the EOMs come from minimizing the error of the TDSE solutions, from the classical mechanics, or from (bohmian) quantum trajectory dynamics.[16] Readers may find useful discussions of the time-dependent variation principle in the context of the basis EOMs in Refs.[14,17–20] We just note here that the variational EOMs, while conceptually rigorous, are, in general, singular and notoriously challenging in implementation (e.g. Ref.[6,21]).

What are the desired features of a dynamical basis, efficiently adapted to a time-evolving wavefunction? In condensed phase, chemical reactions are typically represented by the dynamics in a double-well (reactant/product dynamics) or in a meta-stable (dissociation dynamics) potential in the reaction coordinate, coupled to a bath of the 'spectator' or oscillator modes acting as the energy reservoir. To represent the corresponding time-dependent wavefunctions in a small basis, one wishes for the GBFs to adapt to the flow of the probability density: ideally, some fraction of the GBFs representing an initial wavefunction in the reactant well – all of them with non-negligible amplitudes – will move to the product well (or to the unbound dissociation region) capturing the flow of the probability density. The time-dependence of the basis should be such as to provide adequate space for the evolving wavefunction, which, in general, exhibits an intricate interference dynamics across both wells.

In principle, the 'optimal' time-dependent spatial grid tracking the wavefunction evolu-

tion is given by an ensemble of quantum (bohmian) trajectories (QTs),[16,22] whose dynamics satisfies the continuity of the probability density.[23] While useful for interpretation (e.g.[24,25]), except for the special case of Gaussian solutions to the Schrödinger equation with a parabolic potential, the QT dynamics is characterized by singular forces at and near the wavefunction nodes associated with interference, which makes the exact numerical implementation of the QT approach impractical for general problems. However, within a basis representation, the interference pattern can be described by the time-dependence of the basis expansion coefficients. Thus, during the bound-type dynamics, once the initially localized wavefunction spreads across the low potential energy regions, an accurate basis can become stationary with time. In other words, an efficient basis has to be 'in the right places at the right time', but it is not necessary for the GBFs to track the micro-structure of the time-dependent wavefunction. A specific implementation of these ideas based on the semi-local definition of the trajectory momentum driving the GBF dynamics, is presented in Section 3.2.

A broader question associated with the time-dependent basis representation of wavefunctions explored in this paper, is how to assess the wavefunction accuracy: to determine if a basis change is needed, we have to have a measure of the basis completeness for the wavefunction at hand. Stationary bases offer major simplifications, such as the fact that Hamiltonian and overlap matrix elements have to be computed only once. Furthermore, the basis expansion coefficients can be accurately computed at any time from matrix diagonalization and there are no challenging EOMs for the basis parameters to solve. Naturally, we would like to take advantage of these properties and work in a stationary basis, if it is of manageable size and yields acceptable wavefunction accuracy in the course of time-evolution. Most often the accuracy of dynamics is monitored through the wavefunction's normalization and the energy conservation as analyzed, for example, in Ref.[19] Conservation of the former indicates the accuracy of the time-propagation algorithm. Given a time-independent potential and a sufficiently accurate time-propagation algorithm, the latter remains constant in two cases: (i) the basis is stationary regardless of its completeness, or (ii) the basis is time-dependent

and complete, in a sense of accurately representing the wavefunction at hand. The total energy is also conserved if (iii) the basis parameters are determined according to the Dirac-Frenkel or the Lagrangian variation principles.[26] Thus, energy conservation is not a sufficient measure of the basis completeness in the course of quantum dynamics. Furthermore, in the case of time-dependent Hamiltonians, realized, e.g., in laser-driven molecular systems,[27] or for composite systems, in which energy can be exchanged between subsystems, the energy (of subsystems) is not conserved. An accurate representation for an initially localized wavefunction can become inadequate as the wavefunction spreads in space, e.g. the numerical grid is too short, or the basis is too small, whether it is in configuration, energy or any other space.

In this work, we argue that the average of the Hamiltonian's 'variance' for a given wavefunction is a suitable practical measure of the basis completeness, and analyze its performance using several examples of both time-independent and time- dependent bases. The latter includes application of the CCS and VCS methods and the QTAG dynamics. These three methods are all based on the GBFs whose centers follow EOMs. The CCS trajectories are governed by the classical EOMs, that are independent of the wavefunction; the QTAG dynamics incorporates information on the wavefunction 'flow', while the motion of the VCS trajectories rigorously minimizes the TDSE error and thus conserves energy during the dynamics with time-independent potentials. The proposed measure is closely related to the so-called deviation vector, that compares the difference between the left hand side (the time-derivative of the ansatz wavefunction) and the right hand side (Hamiltonian applied to the wavefunction), that has been mainly applied to the study of the accuracy of Davydov ansätze so far.[20,28–30] By taking the "length" of the deviation vector, in the end, also the expectation of the squared Hamiltonian has to be calculated.[31] In contrast to the measure to be presented in detail below, one also has to calculate time-derivatives of the variational parameters and thus, the deviation-vector measure is quite complex.

The remainder of the paper is organized as follows. Section 2 describes the improved

QTAG dynamics with new semi-local definition for the GBF center time-evolution, and presents the basis completeness measure for non-orthogonal bases. Section 3 contains the numerical illustrations and discussion. Section 4 gives a summary and an outlook. For completeness, the CCS and VCS methods and the key implementation algorithms are given as appendices.

2 Theory

The basis completeness measure is presented in the context of several time-dependent GBF methods: the Coupled Coherent States (CCS) and full Variational Coherent States (VCS) dynamics detailed in Appendices A and B, respectively, and the improved Quantum Trajectory-guided Adaptable Gaussian (QTAG) dynamics. The basis completeness analysis, however, is fully general. For clarity, we work in atomic units ($\hbar = 1$) and consider a one-dimensional particle of mass m whose dynamics is governed by the Hamiltonian operator, $\hat{H}$,

$$\hat{H} = -\frac{\nabla^2}{2m} + V(x), \tag{1}$$

where $V(x)$ is an external time-independent potential. The spatial derivatives are denoted with the gradient symbol, $\nabla := \partial/\partial x$, while the full time-derivatives are denoted by the overdot. Bold upper and bold lower case letters are used to denote matrices and vectors, respectively. The notation $\mathrm{i} = \sqrt{-1}$ is used throughout.

2.1 QTAG basis with semi-local GBF momentum

As in all GBF methods, we start with a wavefunction represented as a superposition of N_b Gaussian functions, $\{g_n\}$,

$$g_n(x,t) := \left(\frac{a_n}{\pi}\right)^{1/4} \exp(-a_n(x-q_n)^2/2 + \mathrm{i}p_n(x-q_n) + \mathrm{i}s_n), \tag{2}$$

$$\psi(x,t) = \sum_{n=1}^{N_b} c_n(t) g_n(x; \boldsymbol{\lambda}_n(t)), \tag{3}$$

where $\{c_n\}$ are the expansion coefficients. In Eq. (3), $\boldsymbol{\lambda}_n(t)$ is a vector of the time-dependent parameters of the n-th GBF, $g_n(x,t)$, which in QTAG includes the center position, q_n, the momentum, p_n defining the linear phase of g_n, and the real width parameter a_n, $\boldsymbol{\lambda}_n(t) = (q_n, p_n, a_n)$. In many dimensions q_n and p_n are generalized to vectors and a_n to a symmetric matrix of appropriate sizes. As discussed in Ref.,[8] each GBF may also include a coordinate-independent phase, s_n. This phase is not uniquely defined, i.e., s_n can be combined with the expansion coefficient c_n, but a good choice, such as relating s_n to the action function of the GBF center trajectory, reduces the temporal oscillations in c_n and allows for larger time-steps during the numerical implementation. In this work, however, we will set $s_n = 0$ for simplicity.

The wavefunction expansion of Eq. (3) is invoked in all GBF methods, such as those mentioned in Section 1. The special features of the QTAG method are: treating the width parameter, a_n, as *real* correlated (in many dimensions) adaptable parameter, and relating the EOMs for the GBF width, a_n, and momentum, p_n, to the quantum trajectory (QT) formalism. The signature feature of the QT framework is identification of the trajectory momentum with the gradient of the wavefunction phase, which leads to the continuity of the probability density associated with each trajectory.[16,22,32] Based on that the EOMs for the QTAG parameters are:

$$p_n := \Im \left(\nabla\psi/\psi \right)\big|_{x=q_n} \tag{4a}$$

$$\frac{\mathrm{d}q_n}{\mathrm{d}t} = \frac{p_n}{m} \tag{4b}$$

$$\frac{\mathrm{d}a_n}{\mathrm{d}t} = -\frac{\nabla p_n}{m} a_n, \tag{4c}$$

They can be interpreted as solutions to the variational equations in the limit of localized

GBFs.[8] The EOMs for the expansion coefficients, $\{c_n\}$,

$$\mathrm{i}\mathbf{S}\dot{\boldsymbol{c}} = \left(\mathbf{H} - \mathrm{i}\dot{\mathbf{S}}\right)\boldsymbol{c}, \tag{5}$$

are the usual variational equations given in terms of the Hamiltonian and the basis overlap matrices, $\mathbf{H}$ and $\mathbf{S}$, respectively,

$$H_{kn} = \langle g_k|\hat{H}|g_n\rangle \tag{6a}$$

$$S_{kn} = \langle g_k|g_n\rangle. \tag{6b}$$

The non-hermitian matrix $\dot{\mathbf{S}}$ contains the full time-derivative of the n-th basis function with respect to its parameters enumerated with the subscript l

$$\dot{S}_{kn} = \langle g_k|\dot{g}_n\rangle, \tag{7a}$$

$$\dot{g}_n = \sum_l \frac{\partial g_n}{\partial \lambda_{n,l}}\dot{\lambda}_{n,l}. \tag{7b}$$

Note, that in QTAG we *do not* solve the bohmian EOM for the momentum of a QT at q,

$$\frac{\mathrm{d}}{\mathrm{d}t}p^{bohm} := -\nabla(V+U)|_{x=q}\,, \tag{8}$$

which involves a possibly singular gradient of the quantum potential $U(x,t)$,

$$U(x,t) := -\frac{1}{2m}\frac{\nabla^2|\psi|}{|\psi|}, \tag{9}$$

formally associated with the division by $|\psi|$ in Eq. (9). Instead, the GBF parameters are updated according to p_n (Eq. (4a)) and its gradient, defined by $\psi(x,t)$ expressed *in a basis*. Furthermore, to regularize the QT dynamics and to change the basis discretely, according to the Basis Orthogonalization/Transformation (BOT) algorithm outlined in Appendix C, Eq. (4a) is implemented with modifications. Even though $\psi(x,t)$ is available analytically as a

basis expansion, Eq. (3), the straightforward implementation of Eq. (4a) may generate large values near the wavefunction nodes, leading to numerically unstable trajectory dynamics. However, because the interference structure of $\psi(x,t)$ is reproducible through to the complex coefficients of the basis expansion, an accurate representation of $\psi(x,t)$ can be achieved with the GBF centers flowing with the probability density in some average sense, i.e. without the exact QTs 'constructing' interference in terms of real quantities, as shown for example in Ref.[33] Previously, in order to regularize the dynamics, the parameters q_n and a_n were updated according to p_n computed either from a convoluted wavefunction, or from the *global* low-order polynomial fit to $\Im(\nabla\psi/\psi)$, rather than from p_n evaluated *locally* at a point, q_n[7,8]). Below we outline a new procedure of computing p_n, in which division by ψ is circumvented and the 'spatial resolution' of the p_n is controlled by a single parameter, β, defined below, controlling the locality of the fitting.

The action of the momentum operator on $\psi(x,t)$ can be expressed as

$$\hat{p}\psi(x,t) = -\mathrm{i}\eta(x,t)\psi(x,t), \tag{10}$$

where $\eta(x,t)$ is complex function,

$$\eta(x,t) := \frac{\nabla\psi(x,t)}{\psi(x,t)}, \tag{11}$$

whose real and imaginary components, $r(x,t)$ and $p(x,t)$ are referred to as the non-classical, $r(x,t)$, and classical, $p(x,t)$, momentum components,

$$r := \frac{\nabla|\psi|}{|\psi|}, \quad p := \nabla(\arg\psi). \tag{12}$$

Let us focus on fitting the complex function η, rather than p. We will define the GBF momentum p_n (and if desired r_n) from the minimization of the q_n-centered error functional,

I_n,

$$I_n = \int |\eta - \tilde{\eta}_n|^2 \, |\psi|^2 w_n dx, \tag{13}$$

where w_n is a Gaussian (or other spatially localized) 'window' function,

$$w_n(x; q_n, \beta) := \sqrt{\frac{\beta}{\pi}} \exp(-\beta(x - q_n)^2). \tag{14}$$

In particular, the linear in x fit centered at q_n, $\tilde{\eta}_n = d_1 + d_2(x - q_n)$, directly yields p_n and ∇p_n – the latter needed to update the GBF width (Eq. (4c)) – as the imaginary parts of the optimal d_1 and d_2, respectively. These fitting parameter values, arranged as a vector, $\boldsymbol{d} = (d_1, d_2)^T$, solve the following system of linear equations for each q_n,

$$\mathbf{M}\boldsymbol{d} = -\boldsymbol{b} \tag{15a}$$

$$b_j = \langle w_n \psi | (x - q_n)^{j-1} | \nabla \psi \rangle \tag{15b}$$

$$M_{ij} = \langle w_n \psi | (x - q_n)^{i+j-2} | \psi \rangle, \quad i, j = \{1, 2\}.$$

Using $|\psi|^2$ as the weighting function in I_n removes division by ψ in the integrand, while the localization of w_n tunes the resolution of $\tilde{\eta}_n$ from low ($\beta \to 0$) to high ($\beta \to \infty$), or from a global to a local fit. Moreover, unlike the convolution of the wavefunction itself,[7] $\boldsymbol{d}$ of Eq. (15a) is exact for a Gaussian wavefunction for any β. If desired, the function r_n and its gradient, defined by the real parts of $\boldsymbol{d}$, can be used to compute the GBF phase s_n.[8] The window parameter can be made GBF-specific, e.g. taken as proportional to its time-dependent width, $\beta_n(t) = a_n(t)/\kappa$, or kept constant in time, $\beta_n = a_n(0)/\kappa$. The choice of κ controls the locality of the fitting procedure, and closeness of p_n to the exact QT momenta. Generalizations to higher order polynomials or other analytical fitting functions, and to non-gaussian window functions are straightforward.

2.2 The basis completeness measure

The accuracy of the basis representation of a time-dependent wavefunction can be assessed as follows. Let us estimate how well the differential time-change of the wavefunction over the time-interval $[0, \tau]$,

$$|\delta\psi\rangle = |\hat{H}\boldsymbol{g}\rangle^T \boldsymbol{c}(\tau), \tag{16}$$

is captured in the initial basis, $\boldsymbol{g}(0)$, by evaluating its orthogonal complement. Using the basis projector, $\hat{P} = |\boldsymbol{g}\rangle \mathbf{S}^{-1} \langle \boldsymbol{g}|$, the basis completeness measure, labeled ϵ, can be defined as,

$$\begin{aligned} \epsilon : &= \langle \delta\psi | (\mathbf{1} - \hat{P}) | \delta\psi \rangle = \langle \psi | \hat{H}^2 | \psi \rangle \\ &- \langle \psi | \hat{H} | \boldsymbol{g} \rangle \mathbf{S}^{-1} \langle \boldsymbol{g} | \hat{H} | \psi \rangle = \boldsymbol{c}^\dagger \boldsymbol{\Delta}_{\mathbf{H}} \boldsymbol{c}. \end{aligned} \tag{17}$$

In Eq. (17), $\mathbf{1}$ is the unit matrix, $\mathbf{H^2}$ is a matrix with the following elements,

$$[\mathbf{H^2}]_{ij} = \langle \hat{H} g_i | \hat{H} g_j \rangle, \tag{18}$$

and $\boldsymbol{\Delta}_H$ denotes what we refer to as the Hamiltonian 'variance' matrix,

$$\boldsymbol{\Delta}_H := \mathbf{H^2} - \mathbf{H}^\dagger \mathbf{S}^{-1} \mathbf{H}. \tag{19}$$

The basis incompleteness associated with the application of $\hat{H}$ to a wavefunction, measured by ϵ, is qualitatively shown in Fig. 1: the changes in the phase-space images (the Wigner transform) of a wavefunction before and after application of the Hamiltonian operator highlight the regions of the coordinate-momentum space that need to be represented by either the stationary or time-dependent bases for accurate wavefunction dynamics. In this illustration the change in the wavefunction is significant and (using ψ as 'basis') the value of ϵ is large, $\epsilon \approx 0.68 \langle \hat{H} \rangle^2$.

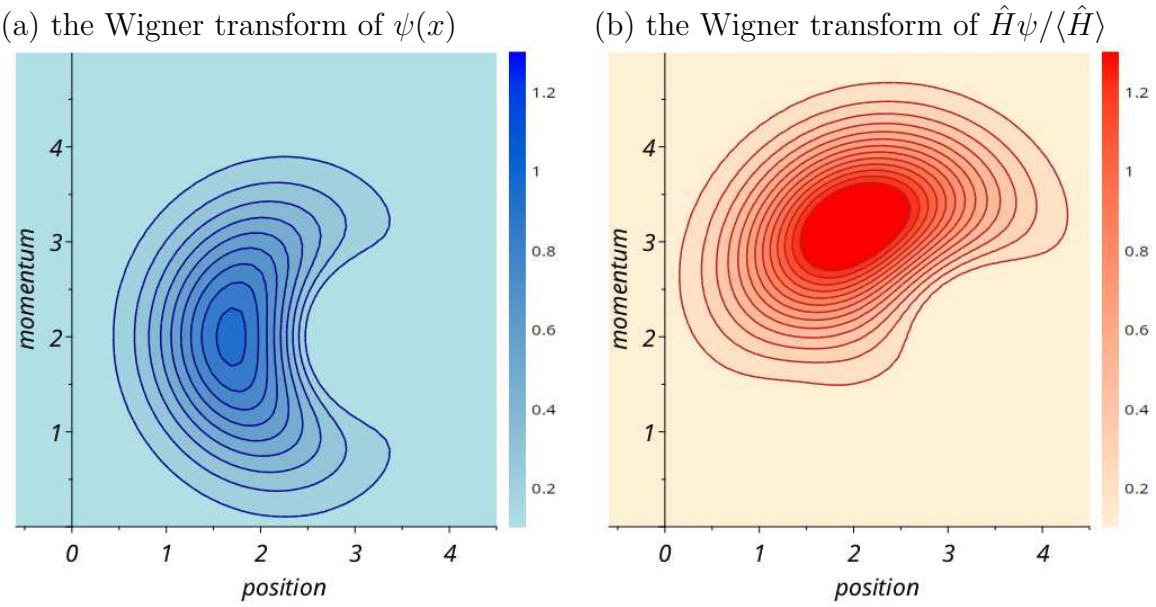

Figure 1: The phase-space representation, i.e. the Wigner transform, of a wavefunction (a) before and (b) after application of $\hat{H}$. The contours are spaced at 0.1 units starting with the value of 0.1. The areas of significant Wigner density have to be 'covered' by the basis. The effect of $\hat{H}$ is quantified by the basis completeness measure, ϵ of Eq. (17). In the limiting case of ψ taken as its own 'basis', the instantaneous basis error is large, $\epsilon \approx 0.68\langle\hat{H}\rangle^2$.

The basis completeness measure is a time-dependent function, $\epsilon = \epsilon(t)$, also referred to as the *instantaneous basis error*. If the basis consists of the Hamiltonian eigenstates, then $\mathbf{\Delta}_H = \mathbf{0}$, and the dynamics error is defined solely by the initial expansion error. Taking the initial expansion of the wavefunction in a basis as 'exact', the propagation error due to the basis incompleteness is proportional to $\tau^2\epsilon$. The value of ϵ can be used to adjust the time-step τ and/or perform the basis update, either according to the EOMs of the basis parameters, or by defining a new basis altogether.

To monitor the effect of the basis incompleteness through time, one can define the *cumulative basis error*, $\chi(t)$:

$$\chi(t) := \int_0^t \epsilon(t')dt'. \tag{20}$$

Let us also recall at this point, that due to the non-local nature of quantum dynamics, the increase in the number of basis functions does not necessarily yield a more accurate solution to the time-dependent Schrödinger equation, which is in contrast to the variational solution

to the time-independent Schrödinger equation.

3 Results and discussion

In this section, we use quantum dynamics of several one-dimensional models, to illustrate the completeness measure applied to the stationary, CCS, VCS and QTAG bases, the latter implemented with the semilocal momentum fitting introduced in Section 2.

3.1 Completeness of the stationary basis

The quartic well. First, let us consider the time evolution of a particle of mass $m = 1$ in the quartic potential defined as,

$$V^{qrt} = V^{HO} + \frac{(x - x_c)^4}{8}. \tag{21}$$

The quartic part of V is centered at $x_c = 1/5$ a$_0$. The quadratic part of the potential V^{HO} is $V^{HO} = x^2/2$ a.u., and the eigenstates of the corresponding harmonic oscillator (HO) are used as the time-independent (Hermite-Gaussian) basis. The initial wavefunction $\psi(x, 0)$ is taken as the ground state of the HO, i.e. the initial expansion coefficients are: $c_1(0) = 1$ and $c_i(0) = 0$ for $i \geq 1$. The time-dependent wavefunction, $\psi(x, t)$, is obtained from the eigenvalues and eigenvectors of the Hamiltonian matrix constructed within the basis of the size $N_b = \{3, 7, 11, 20\}$. The results for the largest basis of 20 functions are taken as 'exact' reference results in the analysis. Besides the instantaneous basis error, $\epsilon(t)$, and the cumulative basis error, $\chi(t)$, of Eqs (17) and (20), respectively, we also examine the wavefunction error, $\sigma(t)$, computed from the overlap of $\psi(x, t)$ constructed in the basis of N_b functions with the reference wavefunction,

$$\sigma := 1 - \langle \psi_{ref} | \psi_{N_b} \rangle. \tag{22}$$

The three time-evolution errors, i.e. ϵ, χ and σ, are shown in Figs 2(a-c), respectively. The basis completeness error exhibits quasi-oscillations as expected for an anharmonic oscillator at low energy, and their amplitude reduces with the increase of N_b. For the four basis sizes listed above, the relative errors defined as $\epsilon/[\mathbf{H^2}]_{11}$, are less than 8.5, 6.7, 2.3 and 0.2%, respectively. The oscillating character of ϵ explains the linear growth of χ with time in Fig. 2(b). The wavefunction errors (σ) shown in Fig. 2(c) for $N_b = \{3, 7, 11\}$, increase essentially linear with time as well, and are below 1.5, 0.25 and 0.01%, respectively.

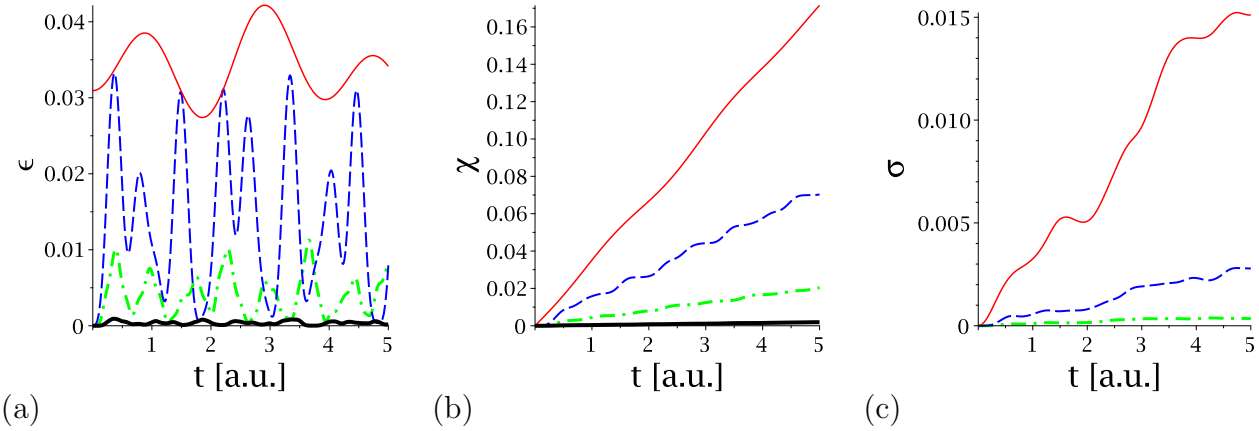

Figure 2: Dynamics in the quartic potential of Eq. (21) employing a Hermite-Gaussian basis of size N_b. (a) The instantaneous, $\epsilon(t)$, and (b) the cumulative, $\chi(t)$, basis errors are shown in appropriate atomic units as functions of time, t, for four basis sizes, $N_b = \{3, 7, 11, 20\}$, as the red solid line, blue dash, green dot-dash and thick black solid line, respectively. In (b) the result obtained with $N_b = 20$ nearly overlaps with the horizontal axis. The unit of $\epsilon(t)$ is E_h^2; the unit of $\chi(t)$ is $\mathrm{E}_h^2\times$(a.u. time). (c) The wavefunction errors, $\sigma(t)$, from the dynamics with $N_b = \{3, 7, 11\}$ functions are shown as the red solid line, blue dash and green dot-dash, respectively. The 'exact' wavefunction is taken from the $N_b = 20$ calculation.

The Morse potential. Figure 3 shows analogous information for the quantum dynamics in the Morse potential, approximating the interaction within the hydrogen molecule. The energy is given in scaled units: the Hamiltonian is multiplied by 918 to have the particle mass $m = 1$. The coordinate x measures the displacement from the equilibrium bond distance of $x_e = 1.4$ a_0. The resulting potential is

$$V^{mrs} = D[\exp(-x) - 1]^2, \tag{23}$$

where $D = 160$ scaled a.u. The results are given for a Gauss-Hermite basis set defined as the eigenstates of the quadratic Taylor expansion of V^{mrs} at $x = 0$. We consider four basis sizes, $N_b = \{4, 6, 8, 14\}$, and the calculation with the largest basis is used as a reference. Let us note, that for $N_b = 14$ the energy of the most oscillatory basis function is equal to twice the dissociation energy, yet 99.99% of its probability density is localized in the region $x < x_e$, or within twice the equilibrium bond distance. Thus, these Hermite-Gauss functions inadequately represent the diffuse character of $\psi(x, t)$ emerging over time, which explains why ϵ and σ in Figs 3(a,c) do not decrease with the larger N_b as strongly as in the previous example of bound motion in the quartic well. Overall, the trends of time-dependent ϵ, χ and σ are similar to those observed for the quartic potential. The relative errors computed as $\epsilon/[\mathbf{H^2}]_{11}$ are less than 4.3, 1.7, 0.7 and 0.4%, respectively. The cumulative error χ is linear in time for all basis sizes; the wavefunction error for $N_b = 6$ and 8 dynamics levels off at longer times, and the two curves show similar trends and amplitudes at shorter times, indicating the limitation of the chosen basis type. Thus, to achieve higher accuracy without significantly increasing the number of the Gauss-Hermite functions it is preferable to use a different basis type, which would include delocalized in space functions to represent the unbound components of the wavefunction, or to use a spatial grid.

Completeness on a grid. Next, let us examine the effect of the grid size on the accuracy of the wavefunction dynamics, using as a model the double well of Ref.,[9]

$$V^{dw} = x^2 \left(b_4 x^2 - b_2 \right). \tag{24}$$

This model with the parameter values of $b_4 = 1/21.6704$ $\mathrm{E}_h\mathrm{a}_0^{-4}$ and $b_2 = 0.5$ $\mathrm{E}_h\mathrm{a}_0^{-2}$ is often used to benchmark the quantum dynamics methods. The wavefunction is computed on a grid of N_p points, equidistant in coordinate space, $x = [x_L, x_R]$. Within the Discrete Variable Representation[34] this grid is equivalent to the *sin*-function basis. Therefore, the accuracy of $\psi(x, t)$ can be evaluated from the matrices $\mathbf{H^2}$ and $\mathbf{H}$ and the projection of

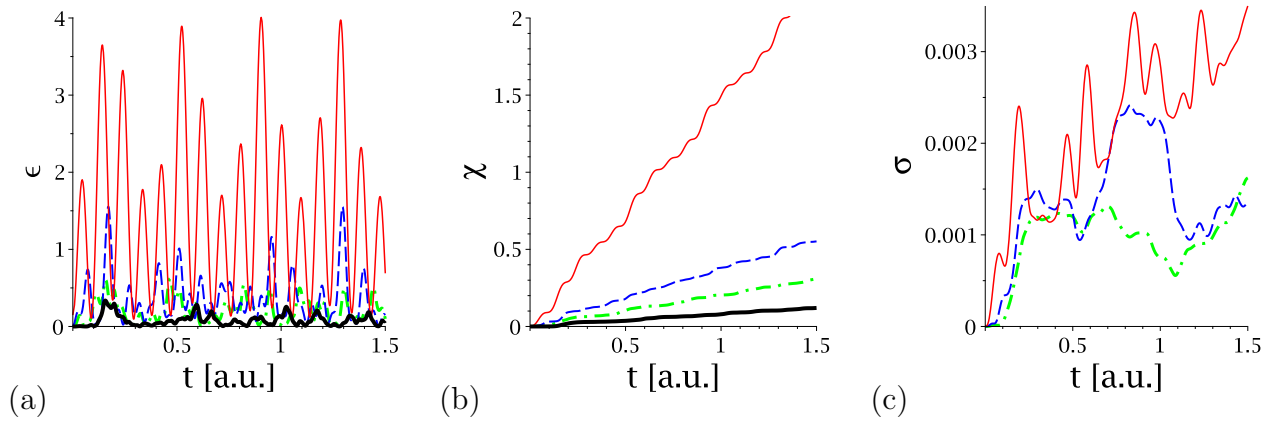

Figure 3: Dynamics in the Morse potential employing a stationary Hermite-Gaussian basis of the size N_b. (a) The instantaneous, $\epsilon(t)$, and (b) the cumulative, $\chi(t)$, basis errors are shown as functions of time, t, are shown in appropriate atomic units for four basis sizes, $N_b = \{4, 6, 8, 14\}$, as the red solid line, blue dash, green dot-dash and thick black solid line, respectively. The unit of $\epsilon(t)$ is E_h^2; the unit of $\chi(t)$ is $\mathrm{E}_h^2 \times$(a.u. time). (c) The wavefunction errors, $\sigma(t)$, from the dynamics with $N_b = \{4, 6, 8\}$ functions are shown as the red solid line, blue dash and green dot-dash, respectively. The 'exact' wavefunction is taken from the $N_b = 14$ calculation.

$\psi(x,t)$ on this basis. The wavefunction initialized in the left well as a coherent Gaussian centered at its minimum is propagated in time using the Split-Operator/Fourier Transform (SOFT) method.[35] The parameters are listed in Table 1. Three values of the right grid boundary, $x_R = \{2.555, 5.110, 7.665\}$ a_0 have been considered; $x_L = -10.22$ a_0 in all cases. The calculations are converged with respect to the grid spacing and time-step. The results are presented for $N_p = 256$.

With this numerical set-up, the short-time dynamics, $t = [0, 4]$ a.u., is sufficient to illustrate the propagation error. Over this time interval less than 3% of the probability density shown in Fig. 4(a) is transferred to the product region (the right well). The instantaneous basis error, $\epsilon(t)$, is shown in Fig. 4(b) on the vertical *log*-scale as a function of time. Three snapshots of the wavefunction amplitude (also on the vertical *log*-scale) tunnelling into the right well are shown in Figs 4(c-e). The errors increase sharply when $|\psi(x,t)|$ becomes appreciable at the grid boundaries, reaching 10^{-8} around $t = 0.2$ and $t = 1.0$ a.u. for $x_R = 2.555$ a_0 and $x_R = 5.110$ a_0, respectively. As seen in Figs 4(c-e), the reflection of $\psi(x,t)$ from

the positive edge of the grid generates 'noise' in $|\psi(x,t)|$ at the negative edge, which is captured by the instantaneous basis error. For the largest grid ($x_R = 7.665$ a$_0$, results shown as green dot-dash) this error remains small, $\epsilon < 10^{-12}$, over $t = [0,4]$ a.u. because the grid is sufficiently large to accommodate the spreading wavefunction. For the smallest grid ($x_R = 2.555$ a$_0$, $|\psi(x,t)|$ represented by the black lines), at $t = 1$ a.u. the noise on the order of 10^{-4} is seen at the left tail of $|\psi(x,t)|$; at later times the propagation errors are clearly seen throughout the full coordinate range. For the intermediate size grid ($|\psi(x,t)|$ plotted with red circles) the wavefunction noise on the left reaches 10^{-5} at $t \approx 2$ a.u., and at $t = 4$ a.u. the interference feature in $|\psi(x,t)|$ in the left well is missing, while $|\psi(x,t)|$ in the right well is still accurate. The instantaneous basis error, ϵ, in Fig. 4(b) is consistent with the trend in the wavefunction accuracy (Figs 4(c-e)).

As seen from the above examples using a stationary basis, the basis completeness errors correlate with the wavefunction errors, and may indicate the basis deficiency. The next illustrations are given for the dynamics performed using time-dependent basis sets, when the assessment of the wavefunction accuracy is more challenging.

3.2 Completeness of time-dependent basis sets

Next, we will analyze the accuracy of the double-well dynamics implemented with different time-dependent GBF methods. This model has been used as a performance test of time-dependent Gaussian basis set methods by many researchers.[9,12,36–38] The challenge here for the trajectory-based methods is to have the GBF centers, initiated in the left reactant well, move to the right product well as the wavefunction accesses this region of space with time.

Coupled Coherent States dynamics. First, we will revisit the double-well model employing the CCS basis.[4] As laid out in Appendix A, the CCS method involves (i) the wavefunction expansion in terms of the GBFs; (ii) Gaussians of time-independent width moving classically; (iii) the variational EOMs for the expansion coefficients; (iv) a normal-ordered

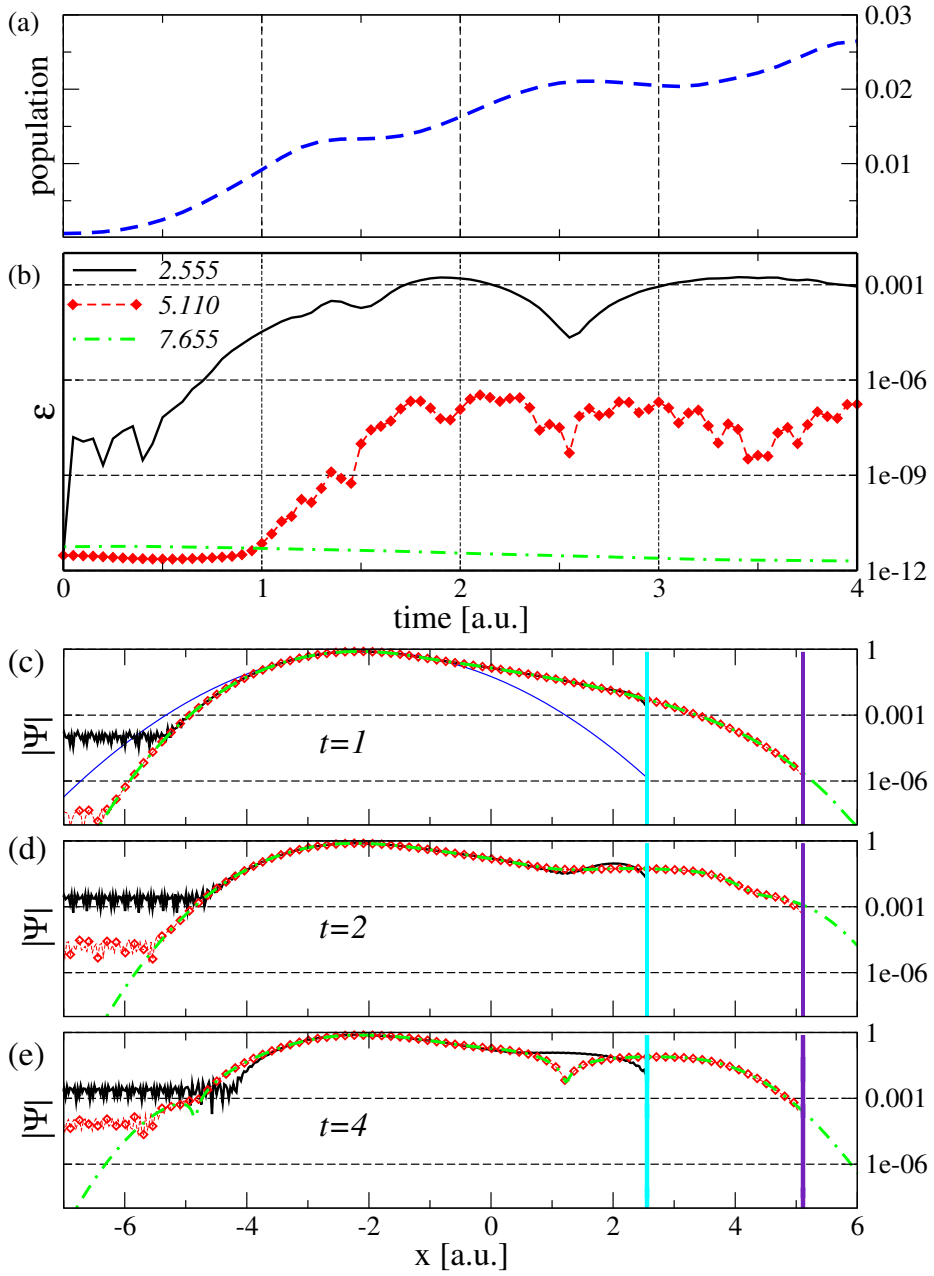

Figure 4: Dynamics in the double well performed on an equidistant asymmetric grid. (a) The population in the right well. (b) The instantaneous basis errors, ϵ, given in the units of E_h^2, evaluated in the *sin*-function basis are given for three values of the right grid boundary x_R, labeled in the legend in the units of a_0, as functions of time. The black solid line, red dash/diamonds and green dot-dash correspond to $x_R = \{2.555, 5.110, 7.665\}$ a_0, respectively. (c-e) The snapshots of $|\psi(x,t)|$ at $t = 1,\ 2$ and 4 a.u., respectively. The same legend applies to panels (b-e). The vertical lines mark $x_R = 2.555$ a_0 (cyan) and $x_R = 5.110$ a_0 (purple). The thin blue line in panel (c) indicates the initial wavefunction.

Hamiltonian, which typically adds a small, often neglected, term to the potential. In CCS dynamics, the (real-valued) initial conditions q_l and p_l typically sample the phase space associated with the Wigner transform of $\psi(x,0)$; formally, the width parameter is equal to the 'coherent' value defined by the frequency of the potential well, $\gamma = m\omega$. Under the assumption of the tight-frame case, the basis overlap matrix in Eq. (5) can be taken as the unit matrix. We refrain from doing so here, however, and use the equations of motion given in Appendix A. Furthermore, because we are dealing with a 1D potential, we also refrain from sampling the initial conditions randomly but take them to be located on a regular rectangular grid in phase space, to be specified below.

As discussed, for example, in Ref.,[38] the double- well model presents a special challenge for the CCS dynamics, because classically moving GBFs corresponding to a low-energy wavefunction do not cross the barrier (even with the ordered Hamiltonian). Therefore, this method may not capture the tunneling dynamics, unless either additional GBFs are placed in the initially unpopulated regions of space or the initial trajectories have enough energy to overcome the barrier. The results presented in Fig. 5 are obtained using 49 GBFs initialized on an equidistantly spaced rectangular grid around the point (-2.33,0) a.u. in phase space with the extension of 1.6 a.u. in q-direction and 2 a.u. in p-direction. The central GBF, which is the zero-momentum Gaussian centered around the minimum of the potential, is the only one that is initially populated. The norm, energy and the basis completeness measure are computed taking the overlap matrix into account. A comparison with the accurate wavefunction computed with the SOFT method and the deviation of the CCS norm from unity, α,

$$\alpha = 1 - |\langle\psi(t)|\psi(t)\rangle| \tag{25}$$

are shown in Figs 5(a,b), respectively. The time interval, $t = [0, 6]$ a.u., shown in Fig. 5 (also in Fig. 6) corresponds to the population transfer to the initially 'empty' well of approximately 2.5%; the population dynamics on a longer time-scale is shown in Fig. 8(c). The panel (c) reveals that energy is quite well conserved to within three significant digits, with the

exact initial value being negative $E = -0.6299$ E$_h$. Finally, Fig. 5(d) shows basis function completeness, presented here for $\langle \hat{H}^2 \rangle$ taken at its initial value of = 0.52244 E$_h^2$, because within the GBF formalism (not going to position and/or momentum representation), we have used the representation of unity in terms of the Gaussians, that appears in the definition of the completeness measure. Under the exact quantum evolution $\langle \hat{H}^2 \rangle$ is constant. The normalization error is below 0.05%, the energy non-conservation is on the order of 1% while variation of ϵ is much more significant reaching $\sim 20\%$. In the CCS method the EOMs for the GBF centers are classical and, therefore, the resulting wavefunction is not fully variational, which along with the instantaneous basis error explains the energy non-conservation. In this example, however, the initial phase space centers are chosen such that a certain fraction of them have enough energy to overcome the barrier and CCS is thus able to capture the tunnelling dynamics at short times.

Fully Variational Coherent States dynamics. To see, if we can do even better by using a fully variational approach, the VCS method reviewed in Appendix B will be applied in the following. We choose the formalism detailed in,[6] because it circumvents certain numerical pitfalls that are due to the non-orthogonality of the basis functions and the fact that they may approach each other arbitrarily closely in the VCS case (not in CCS !).[19] For the short times that we consider, it was not necessary to employ apoptosis, however.

Results analogous to the CCS results from Fig. 5 are presented in Fig. 6. All the accuracy measures are at least one order of magnitude better, however, and most importantly, the basis function completeness measure is almost two orders of magnitude better than in the CCS case. The numerical VCS results have been obtained by using the same number of trajectories as in the CCS case and with identical initial conditions. Detailed timing comparisons have not been performed because both programs run very fast on a modern desktop computer, with the CCS calculations taking less than two seconds and the VCS ones slightly more than two seconds. Also, we would like to mention that in a MATLAB implementation,

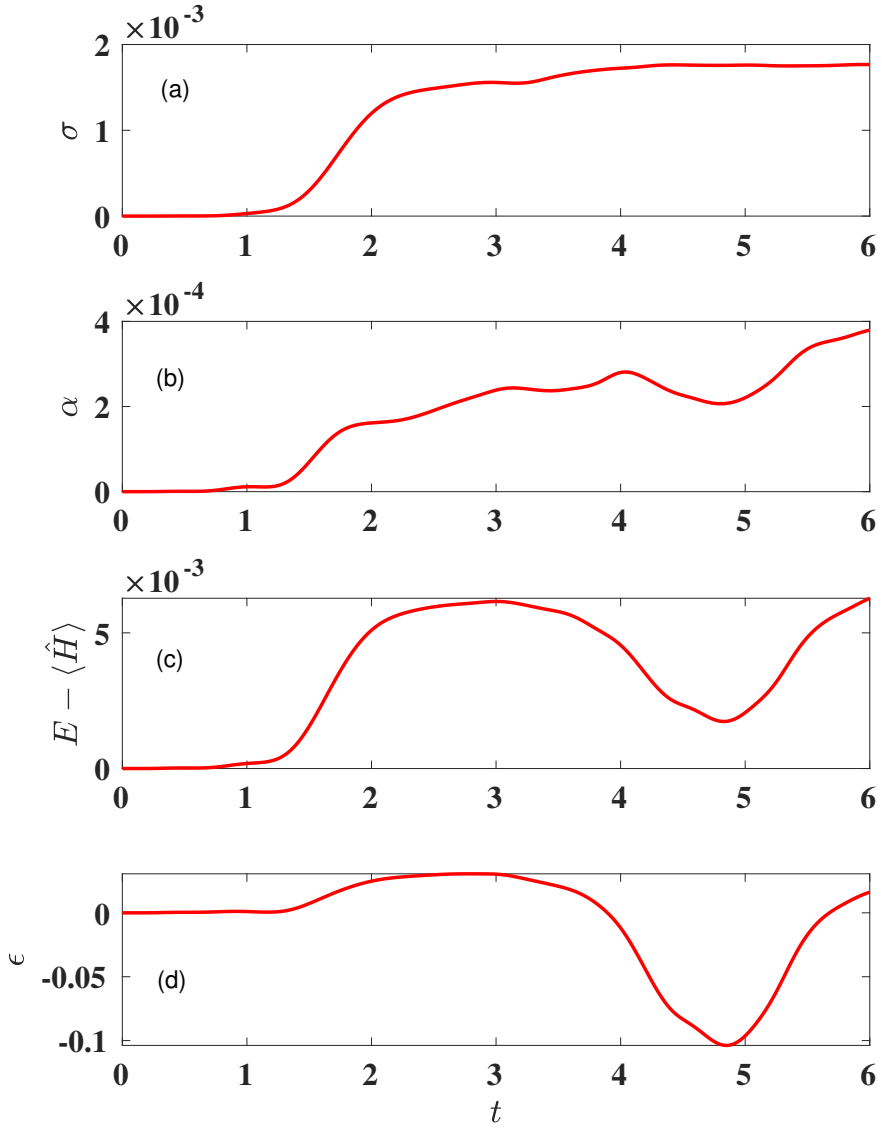

Figure 5: The CCS dynamics in the double well: (a) a comparison with the accurate wavefunction computed with the SOFT method; (b) the quality of norm conservation; (c) the difference between the initial energy and the expectation value of the Hamiltonian given in E_h; (d) the basis completeness as monitored by the quantity ϵ (Eq. 17) given in E_h^2. The time is given in a.u. in all panels.

the relative as well as the absolute tolerance for the ODE solver have been chosen as 10^{-7}. It seems that CCS is not as demanding as VCS in this respect (although, the presented CCS results used the same tolerance parameters). By taking a look at the trajectories (not shown) it turned out that in VCS a larger percentage of trajectories are moving over to the initially unpopulated well in the course of time. This is due to the fact that in VCS case, the trajectories are fully variational and thus, individually, do not conserve energy.

As an additional remark, we would like to mention that we also studied rectangular grids with the same extension but with 25 grid points (less dense grid) as well as with 81 grid points (more dense grid), both using CCS as well as VCS and the results on each level of approximation (not shown) look very similar.

QTAG dynamics. Finally, we will employ the QTAG basis with the semilocal fitting procedure described in Section 2. The initial wavefunction is taken as the minimum energy Gaussian centered in the left well to reduce the low amplitude oscillations in the well and emphasize the tunneling motion. The wavefunction is evolved up to $t = 36$ a.u. which is the time of nearly equal splitting of the probability density between the reactant/product (negative/positive x) regions of space. The model parameters and details of the QTAG calculations are summarized in Table 1. The results are presented for two basis sizes ($N_b = 21$ and $N_b = 29$) and for the Gaussian window functions, described in Section 2.1, of two different widths. The window width parameter, β, is proportional to the time-dependent basis function width parameter a_t; the window functions are referred to as being *narrow* and *wide* for the choice of $\beta = a_t/6$ and $\beta = a_t/30$, respectively. The wide window have significant overlaps with twice as many basis functions as the narrow window. The initial GBF width, a_0, is chosen to give the overlap with the next-neighbor basis function of 0.9.

The key features of the dynamics are illustrated in Fig. 7. The moduli of the initial, $\psi(x, 0)$, and final, $|\psi(x, t)|$, wavefunctions are shown in the bottom and top panels of Fig. 7; the scaled potential is shown in the bottom panel. The probability density flow is visual-

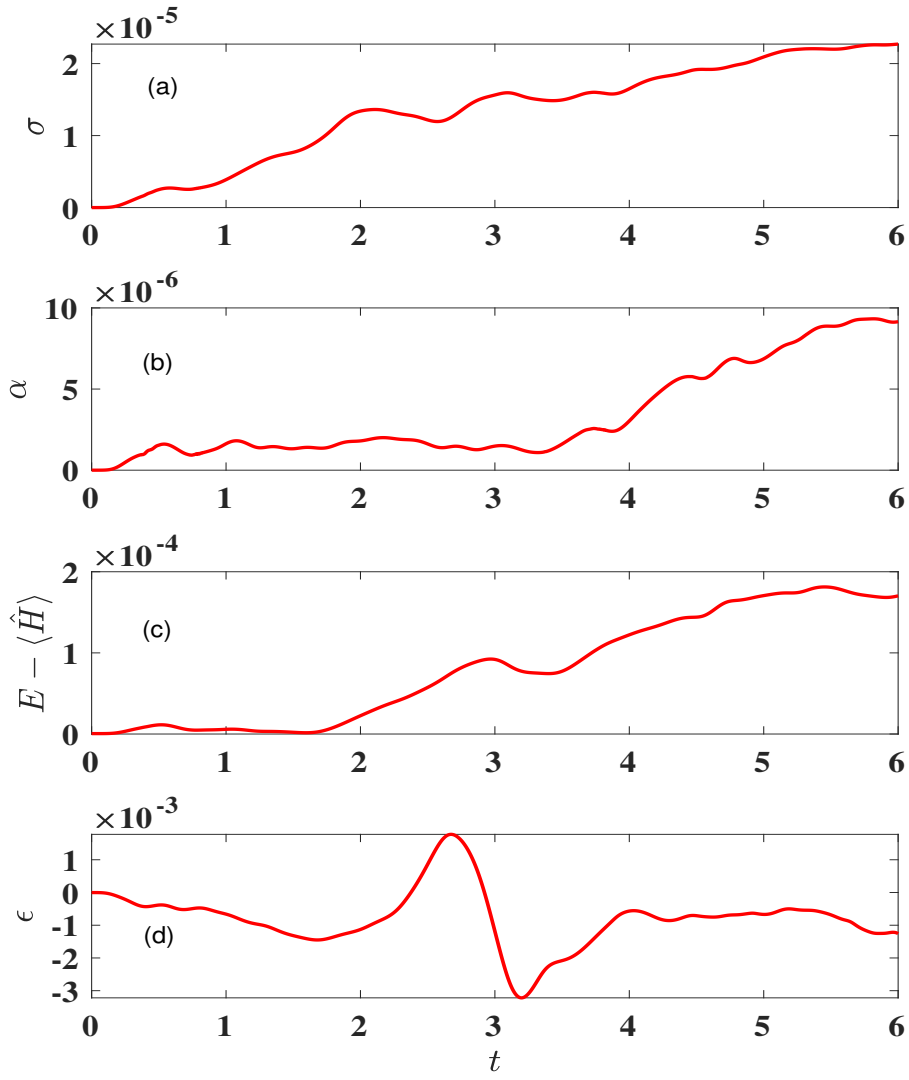

Figure 6: The VCS dynamics in the double well: (a) a comparison with the accurate wavefunction computed with the SOFT method; (b) the quality of norm conservation; (c) the difference between the initial energy and the expectation value of the Hamiltonian (in E_h); (d) the basis completeness as monitored by the quantity ϵ (Eq. 17) given in E_h^2. The time is given in a.u. in all panels.

Table 1: The double well model parameters. In QTAG the GBFs are initialized with the wavefunction density at q_n exceeding $\rho_c = 10^{-5}$. See text for additional details.

The double-well model: $V^{dw} = -b_2x^2 + b_4x^4$		
$b_4 = 1/21.6704$ $E_h a_0^{-4}$	$b_2 = 0.5$ $E_h a_0^{-2}$	$m = 1$ a.u.
$\psi(x,0) = (2\alpha/\pi)^{1/4} \exp\left(-\alpha(x-x_0)^2\right)$		
grid, CCS, VCS	$\alpha = 1.0$ a_0^{-2}	$x_0 = -2.33$ a_0
QTAG	$\alpha = 0.624$ a_0^{-2}	$x_0 = -2.053$ a_0
SOFT parameters		
$N_p = 256$	$x_R = -x_L = 5.61$ a_0	$dx = 0.044$ a_0
QTAG parameters		
$N_b = 29$	$a_0 = 12\alpha$	$\beta = a_t/6,\ a_t/30$
$N_b = 21$	$a_0 = 7.64\alpha$	$\beta = a_t/6,\ a_t/30$

ized through a set of QTs (shown as blue solid lines), reconstructed from the wavefunction computed with SOFT method. These trajectories, sampling $\psi(x,0)$ of appreciable amplitude ($|\psi(x,q_n)|^2 > 10^{-5}$) are equidistant at $t = 0$, and their separation correlates with the changes of the probability density with time. We see that during short times ($t < 4$ a.u.) three of the QTs near the top of the barrier move to the product well and stay there. These trajectories can be interpreted as representing the high-energy components of $\psi(x,0)$. As time progresses, three more trajectories move from the left to the reactant to the product region; these QTs represent the tunneling components of the wavefunction, which should add up constructively to describe build up of the probability density in the right well. Seven of the blue trajectories exhibit small amplitude oscillations in the left well throughout the entire propagation time; these trajectories represent the surviving reactant well population of about 50%. Comparing the QTs to the QTAG GBF centers (half of which as shown for the calculation with $N_b = 29$ and 'narrow' window function, $\beta = a_t/6$), we observe that the latter trajectories exhibit a similar to QTs pattern of the trajectory drift into the product well. The GBF transfer between the wells, however, proceeds more smoothly compared to QTs due to the semilocal 'averaging' of the trajectory momenta derived from the wavefunction.

The basis completeness measure, basis errors and the propagation accuracy are illustrated in Fig. 8. The best energy conservation (Fig. 8(a)) is seen for largest basis size for both

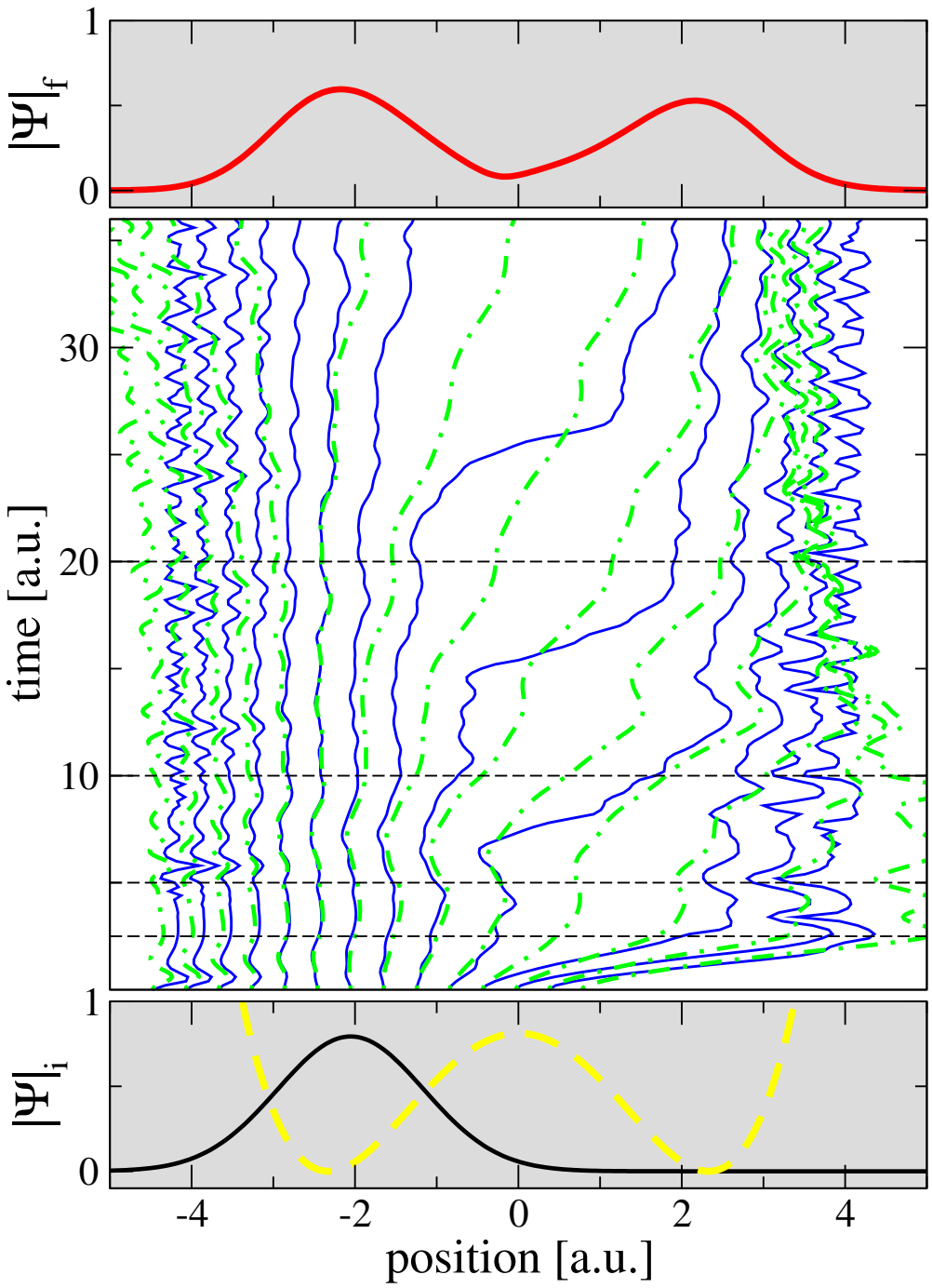

Figure 7: Dynamics in the double-well potential, performed with the QTAG bases. Selected GBF centers (green dot-dash) and QTs (blue solid line) are shown in the central panel. The initial and final $|\psi|$ ($t = 0$ and $t = 36$ a.u.) are shown as the solid lines in the bottom and top panels, respectively. The potential (out of scale) is shown as the yellow dash in the bottom panel. All panels have the same horizontal axis. The horizontal dashes indicate the GBF stopping times, $t = [2.5, 5, 10, 20]$ a.u. for the dynamics depicted in Fig. 10.

wide and narrow window functions, which correlates with the better accuracy of the final wavefunction at $t = 36.0$ a.u. (Fig. 8(d)). At this time the wavefunction is nearly equally split between the two wells as seen in Fig. 8(c). The total energy in both calculations with the smaller bases have sizable regions of near constant values; however, since the propagation errors at short times have a non-linear effect on the accuracy at later times, the energy conservation alone is not a sufficient measure of the dynamics accuracy. The cumulative basis error, $\chi(t)$, is shown in Fig. 8(b). The large basis/wide window dynamics has the smallest error over $t = [0, 36]$ a.u., but the large basis/narrow window dynamics is the most accurate at short times for both basis sizes. Figure 9(a) illustrates the instantaneous basis error $\epsilon(t)$ for $t = [0, 4]$ a.u. on the *log*-scale. The wavefunction amplitude snapshots for $t = 1.0$ and 2.0 a.u are given in Fig. 9(b,c), respectively. The increase in $\epsilon(t)$ correlates with the error in the transmitted wavefunction. The narrow-window fitting leads to more accurate wavefunction description for both basis sizes (green dash and thin solid black line), though subsequent cumulative error remains nearly unchanged in the wide-window dynamics. Overall, in this example both the energy conservation and the basis completeness measure are well correlated with the dynamics accuracy.

Finally, let us examine the basis errors and the energy conservation as we switch from the time-dependent to the time-independent QTAG basis. This switch is straightforward within the BOT algorithm described in Appendix C. The results of QTAG dynamics with the large basis/narrow fitting window are shown in Fig. 10 for the GBFs that stopped changing at times $t = \{20, 10, 5, 2.5\}$ a.u. The full propagation time is $t = 36$ a.u. as before. The modulus of the final wavefunction, the relative energy error, the cumulative error, χ, and the basis completeness error, ϵ are presented in Figs 10(a-d), respectively. The panels (b) and (d) correspond to the running averages over 0.5 and 1.0 units of time. For all dynamics the energy is conserved with the accuracy of better than 0.01% at very short times ($t < 2$ a.u.) and at all times when the basis becomes stationary. The smallest energy error is seen for the GBFs that were stopped at 2.5 a.u., by which time the GBFs are already smeared

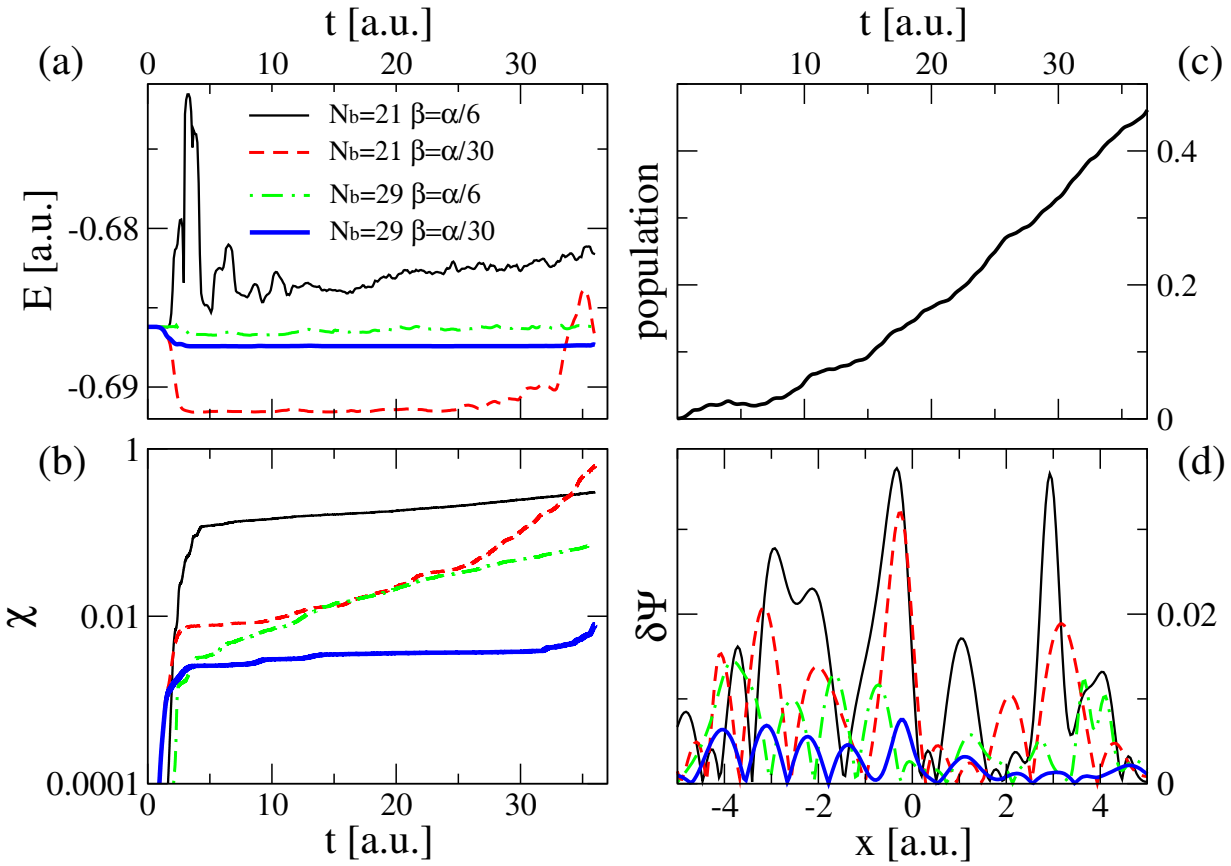

Figure 8: Dynamics in the double-well potential performed with the QTAG bases. (a) The total wavefunction energy, E, and (b) the cumulative basis error, χ, (in the atomic units of energy$^2\times$time) as functions of time. (c) The population of the right well as a function of time, obtained with the SOFT method. (d) The wavefunction amplitude error with respect to the SOFT result, $\delta\psi$, at $t = 36$ a.u. The legend in panel (a) applies to panels (a,b,d), all showing the results for two basis sizes, $N_b = 21$ and $N_b = 29$, paired with the narrow ($\beta = \alpha/6$) and wide ($\beta = \alpha/30$) fitting window; α and β are the widths parameters of the GBFs and the window function, respectively.

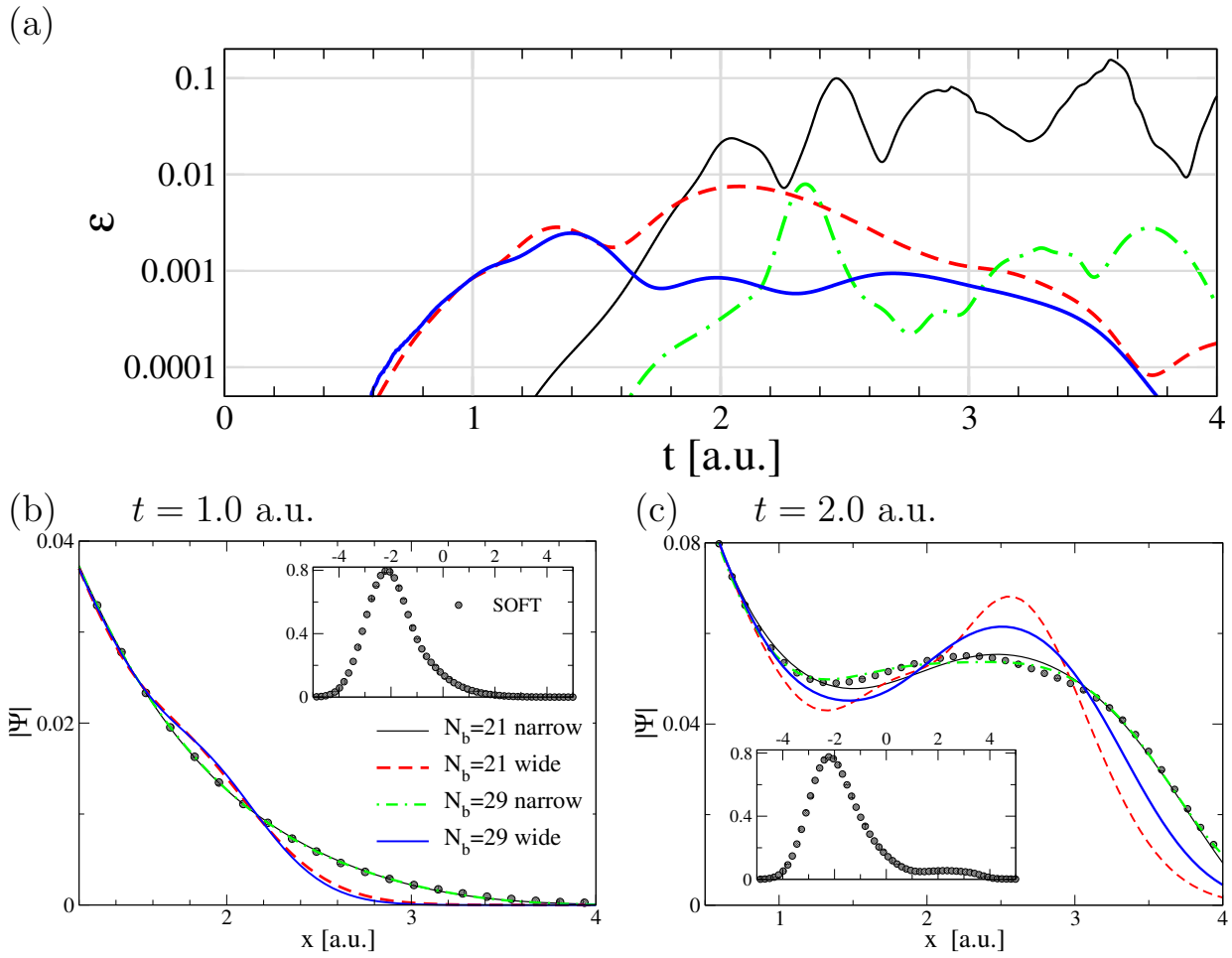

Figure 9: Short-time dynamics in the double-well potential within the QTAG basis. (a) The instantaneous basis error, ϵ, as a function of time t. The modulus of the bifurcating wavefunction at (b) $t = 1$ and (c) $t = 2$ a.u. The inserts show $|\psi(x,t)|$ as functions of x on the full vertical and horizontal range. The same legend is used in all panels. The running averages of ϵ over 0.1 a.u. of time are shown in panel (a).

over both wells as seen in Fig. 7. However, as seen in Fig. 10(d), in this case the ensuing dynamics is characterized by the increasing with time basis completeness error, shown on log-scale. This behavior is seen in the cumulative error in Fig. 10(c) (note the log-scale for both axes), and in the accuracy of the final wavefunction, whose transmitted part is shown in Fig. 10(a). The basis completeness errors with the fully time-dependent GBFs or with those stopped at time 5, 10 or 20 a.u. are of comparable accuracy, with the basis frozen at $t = 5$ a.u. yielding the smallest errors. The final wavefunctions shown in Fig. 10(a) exhibit some discrepancies in the low amplitude regions, which are the high energy walls of the potential, but all of these wavefunctions are in significantly better agreement with the exact result, compared to the result of the minimally evolved basis stopped at $t = 2.5$ a.u. Note that $\psi(x,t)$ is shown for $x > 0$ on log-scale, thus the apparent discrepancy with the exact result is not proportional to the basis completeness measure, ϵ, defined as the TDSE solution error on full space. The definition of ϵ can be easily adapted to a subspace to serve as a more local measure, if desired. Quantum dynamics itself, however, is inherently non-local, and small 'local' ϵ may be a poor predictor of the wavefunction dynamics in general.

4 Conclusions

In this paper we have discussed a practical measure of the accuracy of a time-dependent wavefunction, important for the development of efficient time-dependent basis sets. Such bases are expected to maintain an accurate representation of the time-evolved wavefunction with a reasonable number of the basis functions, by adapting them to the wavefunction solving the time-dependent Schrödinger equation. A seemingly straightforward task of the basis accuracy assessment runs counter to the 'classical' association of the energy conservation with the accuracy of dynamics: in quantum dynamics the energy is conserved for a complete time-dependent basis, for any time-independent basis, or for variational basis sets evolving according to the Dirac-Frenkel variation principle. In the present manuscript we argue that

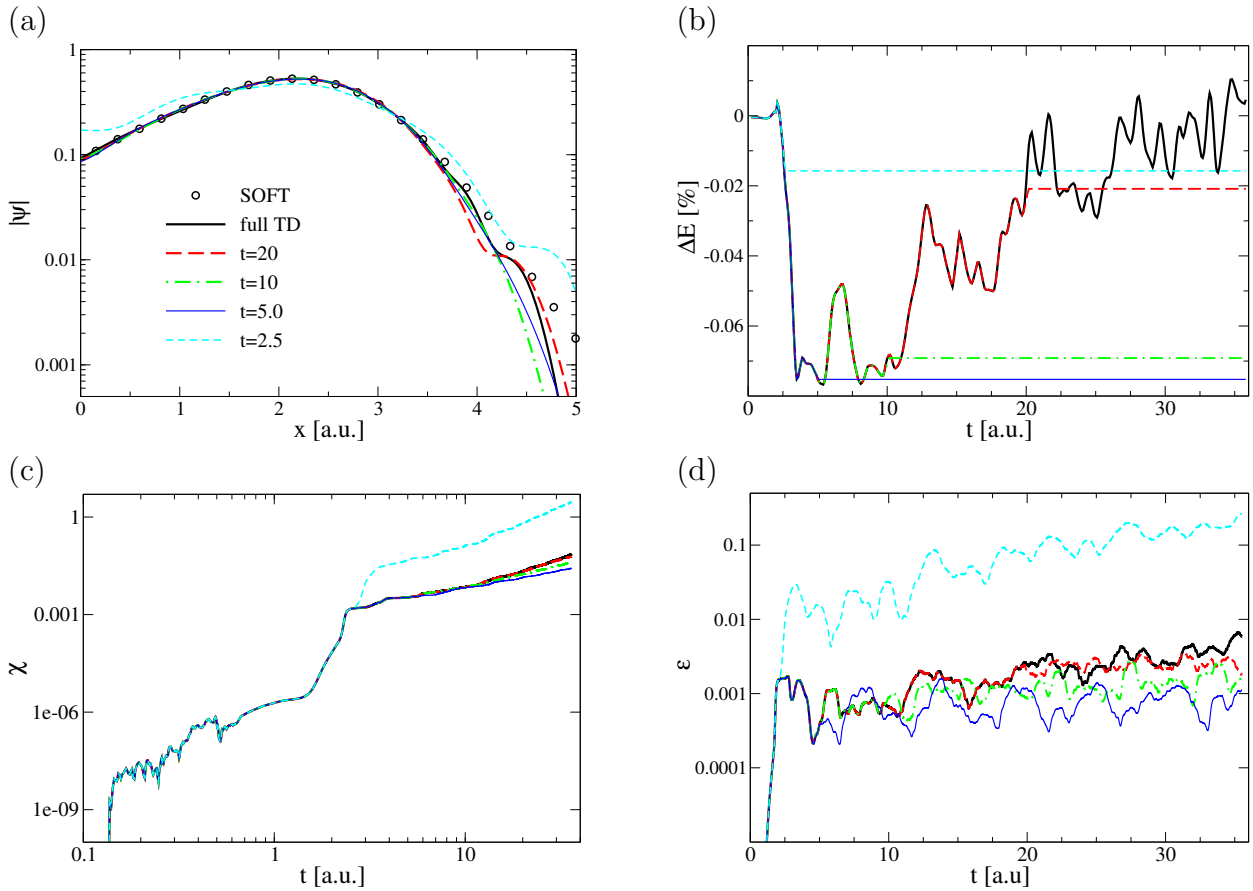

Figure 10: Dynamics in the double well based on QTAG functions stopped at intermediate times of the propagation. (a) The modulus of the final wavefunction ($t = 36$ a.u.) in the product side of the potential. (b) The relative energy error, $\Delta E = (E_0 - E_t)/|E_0|$, (c) the cumulative basis error, χ, and (d) the instantaneous basis error, ϵ, as functions of time. The untis of χ are $\mathrm{E}_h^2 \times$(a.u. time) and of ϵ are E_h. The exact SOFT result are shown with circles. The QTAG results obtained with the fully time-dependent GBFs and with the GBFs stopped at $t = 20,\ 10,\ 5$ and 2.5 a.u. are shown as thick black solid lines, red long dashes, green dot-dashes, thin blue lines and cyan short dashes, respectively. The legend in panel (a) applies to all panels. The results in (b) and (d) are shown as running averages over 0.5 a.u. and 1.0 a.u. of time for clarity.

the average Hamiltonian 'variance', $\epsilon = \langle \hat{H}^2 \rangle - \langle \hat{H}\hat{P}\hat{H} \rangle$, where $\hat{P}$ is the resolution of identity in a basis, is a rigorous and practical basis completeness measure for the wavefunction at hand. Moreover, the presented basis completeness measure is applicable to the dynamics with time-dependent potentials, as well as to the dynamics of subsystems of interacting, composite systems, where the energy is not conserved.

Our analysis is based on several examples of both time-independent as well as time-dependent bases. For the time-independent bases, we have demonstrated how the basis completeness measure correlates with the wavefunction accuracy: the measure decreases with the increase of the basis size, and its time-dependence indicates certain deficiencies of the basis, such as short grid or the lack of delocalized basis functions. The analysis of the basis completeness measure is based on the results obtained with three time-dependent GBF methods, i.e. the Coupled and Variational Coherent States and the QTAG basis. In the double-well example – the prototype model of reactive dynamics in condensed phase – the coherent state basis quickly (5% of the well-to-well population transfer) started to loose accuracy when the GBFs centers moved classically, and the accuracy was improved by around two orders of magnitude once the classical EOMs were replaced by the fully variational EOMs. The QTAG dynamics, that can be viewed as guided but not fully defined by the highly challenging in implementation variational EOMs, was analyzed up to nearly equal splitting of the well populations. The new semi-local algorithm for updating the GBF parameters yielded non-classical trajectories which exhibited the desired transfer between the two wells, necessary to capture the tunneling dynamics within a small basis. We also demonstrated that once the initial wavefunction was delocalized between the two wells, one could freeze the basis function without loss of accuracy, which has considerable practical advantages.

In summary, the basis completeness measure, defined in terms of the Hamiltonian 'variance' matrix, provides a faithful and practical way of assessing accuracy of quantum dynamics regardless of the basis type (time-dependent or time-independent) or basis construction

(through EOMs or the wavefunction sampling), which will be helpful for the choice of efficient and accurate bases, method development and realistic chemical applications. We note, however, that due to the non-local in space and non-linear in time nature of quantum dynamics, application of this particular measure and, most likely, of other instantaneous (defined for a given wavefunction expanded in a basis) measures by imposing a certain criterion on their value at each time step, will not guarantee a predefined long-time accuracy of the wavefunction.

5 Acknowledgment

This material is based upon work supported by the National Science Foundation of U.S.A. under Grant No. CHE-2308922. SG acknowledges support from the MPIPKS during her stay at the Institute (March-July, 2023). The authors are grateful to Prof. Jan-Michael Rost and Dr. Yulong Qiao for many illuminating discussions.

A Coupled coherent states method

In the coupled coherent states (CCS) method of Shalashilin and Child,[39] the ansatz for the wavefunction as a sum over coherent states in most conveniently written in the form

$$|\psi(t)\rangle = \sum_{l=1}^{N_b} c_l(t)|z_l(t)\rangle. \tag{26}$$

In this as well as in the following appendix, the coherent states $|z\rangle$, which in position as well as in momentum representation are Gaussians (however, with a different phase convention as in Eq. (2), see, e.g.,[14]), are denoted by their complexified center variables

$$z_l(t) = \frac{\gamma^{1/2} q_l(t) + \mathrm{i}\gamma^{-1/2} p_l(t)}{\sqrt{2}}, \tag{27}$$

with a width parameter γ that is fixed in time (and thus has another symbol than the width parameter used in the main text, which is time-dependent). Characteristic for the CCS method, the $z_l(t)$ are uncoupled classical trajectories following Hamilton's equations (note that the equation below has a real and an imaginary part)

$$\mathrm{i}\partial_t z = \partial_{z^*} H_{\mathrm{ord}}(z, z^*), \tag{28}$$

that can be derived by applying the time-dependent variational principle (TDVP) to the ansatz with multiplicity $N_b = 1$.[5] The ordered Hamiltonian is gained by expressing the Hamilton operator in terms of harmonic oscillator creation and annihilation operators, followed by a normal ordering (in a product all appearances of $\hat{a}^\dagger$ precede those of $\hat{a}$) and the subsequent calculation of the matrix elements between the coherent states.

The equations of motion for the coefficients are then derived from the application of the TDVP to the full ansatz and are linear, coupled differential equations of the form

$$\mathrm{i}\sum_{l=1}^{N_b}\langle z_k(t)|z_l(t)\rangle\dot{c}_l(t) = \sum_{l=1}^{N_b}\tilde{H}_{kl}(t)c_l(t), \tag{29}$$

with the time-dependent matrix elements

$$\begin{aligned}\tilde{H}_{kl}(t) = \langle z_k(t)|z_l(t)\rangle\Bigg[&H_{\mathrm{ord}} - \\ &\frac{1}{2}\left(z_l(t)\frac{\partial H_{\mathrm{ord}}}{\partial z_l} - \frac{\partial H_{\mathrm{ord}}}{\partial z_l^*}z_l^*(t)\right) - z_k^*(t)\frac{\partial H_{\mathrm{ord}}}{\partial z_l^*}\Bigg],\end{aligned} \tag{30}$$

and where an overlap matrix element appears on both sides of the equation. We stress that it may not be cancelled because the multiplication in Eq. (30) is an elementwise multiplication. For the inversion of the overlap matrix in a numerical implementation we thus employ a regularization in the form of the addition of a unit matrix multiplied by 10^{-8} to the overlap. Furthermore, the partial derivatives of the ordered Hamiltonian may be replaced by the left hand side of the classical equation of motion, Eq. (28). We found that there is only a

marginal difference in the performance of the code due to this change, however.

B Variational coherent states method

In the variational coherent states (VCS) method,[14] the same ansatz as in Eq. (26) is made for the wavefunction. Now, however, both the "trajectories", i.e., the coherent state parameters, as well as the coefficients are derived from the TDVP applied to the full ansatz with multiplicity N_b. This leads to the following coupled, nonlinear equations of motion:

$$\mathrm{i}\sum_{l=1}^{N_b}\langle z_k|z_l\rangle\left[X_l + c_l z_k^* \dot{z}_l\right] = \langle z_k|\hat{H}|\Psi(t)\rangle, \tag{31}$$

$$\mathrm{i}c_k^*\sum_{l=1}^{N_b}\langle z_k|z_l\rangle\left[z_l X_l + c_l(1+z_k^* z_l)\dot{z}_l\right] = c_k^*\langle z_k|\hat{a}\hat{H}|\Psi(t)\rangle, \tag{32}$$

where the definition

$$X_k := \dot{c}_k + c_k\left[-\frac{1}{2}\left(z_k\dot{z}_k^* + \dot{z}_k z_k^*\right)\right] \tag{33}$$

was used. The general idea of the fully variational solution has a long history, reviewed, e.g., in,[3,5,14] where additional references can be found. One decisive feature of the present approach, developed in,[6] is the introduction of the vector of variables X_k, that together with the set of z_k fulfills a linear system of equations (not differential equations!) that are solved according to the general strategy laid out in,[6] making the (nonlinear) differential equations explicit.

The presentation in[6] is given for an arbitrary number of degrees of freedom and thus may be hard to grasp at first glance. In order for this presentation to be self-contained, we review the procedure for a single degree of freedom in the following. To this end, we first

define four vectors of length N_b (the multiplicity):

$$\mathbf{x} = (X_1, \ldots, X_{N_b}) \tag{34}$$

$$\mathbf{y} = (\dot{z}_1, \ldots, \dot{z}_{N_b}) \tag{35}$$

$$\mathbf{c} = (c_1, \ldots, c_{N_b}) \tag{36}$$

$$\mathbf{z} = (z_1, \ldots, z_{N_b}) \tag{37}$$

The equations of motion can then be brought in standard form

$$\mathrm{i} \begin{pmatrix} \mathbf{S} & \mathbf{B} \\ \mathbf{B}^\dagger & \mathbf{D} \end{pmatrix} \begin{pmatrix} \mathbf{x}^{\mathrm{T}} \\ \mathbf{y}^{\mathrm{T}} \end{pmatrix} = \begin{pmatrix} \mathbf{r} \\ \mathbf{s} \end{pmatrix}, \tag{38}$$

where

$$S_{lk} = \langle z_l | z_k \rangle \tag{39}$$

are elements of the Hermitian $N_b \times N_b$ overlap matrix and

$$\mathbf{B} = [\mathbf{z}^\dagger \otimes \mathbf{c}] \circ \mathbf{S}, \tag{40}$$

as well as

$$\mathbf{D} = \left(\mathbf{z}^\dagger \otimes \mathbf{z} + 1_{N_b \times N_b}\right) \circ (\rho \circ \mathbf{S}) \tag{41}$$

are $N_b \times N_b$ matrices and $1_{N_b \times N_b}$ denotes an $N_b \times N_b$ matrix full of ones, whereas $\rho = \mathbf{c}^\dagger \otimes \mathbf{c}$ is the density matrix. The symbol $\otimes$ denotes tensorial multiplication, while $\circ$ stands for elementwise multiplication of matrices.

The vectors on the RHS of Eq. (38) are finally given by

$$\mathbf{r} = [\mathbf{H} \circ \mathbf{S}]\mathbf{c}^{\mathrm{T}}, \tag{42}$$

$$\mathbf{s} = \Big(\rho \circ \mathbf{S} \circ \mathbf{H}\Big)\mathbf{z}^{\mathrm{T}} + \left(\rho \circ \mathbf{S} \circ \bar{\mathbf{H}}\right)_2, \tag{43}$$

where the matrix elements $H_{lk} = H_{\rm ord}(z_l^*, z_k)$ are given by the ordered Hamiltonian, whereas the $\bar{H}_{lk} = \frac{\partial H_{\rm ord}(z_l^*, z_k)}{\partial z_l^*}$ are given by its derivatives. Finally, the lower index 2 in the last equation above indicates summation over the second index of the matrix in brackets.

With the $2N_b \times 2N_b$ system of linear equations solved, an explicit system of coupled differential equations is established that can finally be tackled by standard (Runge-Kutta) techniques.

C Basis orthogonalization/transformation (BOT) propagator.

The BOT scheme[8] of solving the TDSE in a non-orthogonal basis $\{\mathbf{g}\}$ consists of two steps. The wavefunction is expanded as

$$|\psi\rangle = \mathbf{c}^T|\mathbf{g}\rangle.$$

The elements of the basis overlap matrix, $\mathbf{S}$, are

$$S_{ij} := \langle g_i|g_j\rangle.$$

When appropriate, the time will be indicated as an argument of functions, while the spatial arguments will be omitted.

(1) Starting at time $t = 0$, evolve the expansion coefficients $\mathbf{c}(0)$ up to time τ in a fixed basis defined, $\mathbf{g}(0)$,

$$\mathbf{c}(0) = (\mathbf{S}(0))^{-1}\langle\mathbf{g}(0)|\psi(0)\rangle, \tag{44}$$

according to

$$\mathrm{i}\mathbf{S}\dot{\mathbf{c}} = \mathbf{H}\mathbf{c}, \tag{45}$$

using the generalized column-eigenvectors (arranged as columns of the matrix $\mathbf{Z}$) and eigenvalues, λ_i, of the Hamiltonian matrix $\mathbf{H}$, $H_{ij} = \langle g_i|\hat{H}|g_j\rangle$. The eigenvalues form the diagonal

matrix $\mathbf{\Lambda}$),

$$\mathrm{i}\mathbf{S}\dot{\mathbf{c}} = \mathbf{H}\mathbf{c}, \quad \mathbf{H}\mathbf{Z} = \mathbf{S}\mathbf{Z}\mathbf{\Lambda}. \tag{46}$$

The expansion coefficients of $\psi(\tau)$ represented in the original basis $\mathbf{g}(0)$ are:

$$\mathbf{c}(\tau) = \mathbf{Z}\exp(-\mathrm{i}\mathbf{\Lambda}\tau)\mathbf{Z}^{\dagger}\mathbf{S}_0\mathbf{c}(0). \tag{47}$$

(2) Update the basis now labeled $\{\mathbf{g}(\tau)\}$ (using the EOMs, rehashing or some other procedure), compute the new overlap matrix $\mathbf{S}(\tau)$ and the new/old basis overlap matrix $\mathbf{T}(\tau, 0)$, and project the wavefunction $\psi(\tau)$ into the new basis:

$$\mathbf{S}(\tau)\tilde{\mathbf{c}}(\tau) = \mathbf{T}(\tau, 0)\mathbf{c}(0), \quad [T(\tau, 0)]_{ij} = \langle g_i(\tau)|g_j(0)\rangle. \tag{48}$$

(3) Assign $\mathbf{c}(\tau) := \tilde{\mathbf{c}}(\tau)$, compute the Hamiltonian matrix in the new basis, $\mathbf{H}(\tau)$, and repeat the steps (1-3) for $\tau \to 2\tau$ and so on until the final time is reached.

References

(1) V. A. Rassolov and S. Garashchuk Computational Complexity in Quantum Chemistry. *Chem. Phys. Lett.* **2008**, *464*, 262–264.

(2) Burghardt, I.; Nest, M.; Worth, G. A. Multiconfigurational System-Bath Dynamics Using Gaussian Wave Packets: Energy Relaxation and Decoherence Induced by a Finite-Dimensional Bath. *J. Chem. Phys.* **2003**, *119*, 5364–5378.

(3) Richings, G.; Polyak, I.; Spinlove, K.; Worth, G.; Burghardt, I.; Lasorne, B. Quantum Dynamics Simulations Using Gaussian Wavepackets: The VMCG Method. *International Reviews in Physical Chemistry* **2015**, *34*, 269–308.

(4) Shalashilin, D. V.; Child, M. S. Real Time Quantum Propagation on a Monte Carlo

Trajectory Guided Grids of Coupled Coherent States: 26D Simulation of Pyrazine Absorption Spectrum. *J. Chem. Phys.* **2004**, *121*, 3563–3568.

(5) Shalashilin, D. V.; Burghardt, I. Gaussian-Based Techniques for Quantum Propagation from the Time-Dependent Variational Principle: Formulation in Terms of Trajectories of Coupled Classical and Quantum Variables. *J. Chem. Phys.* **2008**, *129*, 084104.

(6) Werther, M.; Großmann, F. Apoptosis of Moving Nonorthogonal Basis Functions in Many-Particle Quantum Dynamics. *Phys. Rev. B* **2020**, *101*, 174315.

(7) Gu, B.; Garashchuk, S. Quantum Dynamics with Gaussian Bases Defined by the Quantum Trajectories. *J. Phys. Chem. A* **2016**, *120*, 3023–3031.

(8) Dutra, M.; Wickramasinghe, S.; Garashchuk, S. Quantum Dynamics with the Quantum Trajectory-Guided Adaptable Gaussian Bases. *J. Chem. Theory Comp.* **2020**, *16*, 18–34.

(9) Wu, Y.; Batista, V. S. Quantum Tunneling Dynamics in Multidimensional Systems: A Matching-Pursuit Description. *J. Chem. Phys.* **2004**, *121*, 1676–1680.

(10) Koch, W.; Frankcombe, T. J. Basis Expansion Leaping: A New Method to Solve the Time-Dependent Schrodinger Equation for Molecular Quantum Dynamics. *Phys. Rev. Lett.* **2013**, *110*.

(11) Saller, M. A. C.; Habershon, S. Basis Set Generation for Quantum Dynamics Simulations Using Simple Trajectory-Based Methods. *J. Chem. Theory Comput.* **2015**, *11*, 8–16.

(12) Saller, M. A. C.; Habershon, S. Quantum Dynamics with Short-Time Trajectories and Minimal Adaptive Basis Sets. *J. Chem. Theory Comput.* **2017**, *13*, 3085–3096.

(13) Garashchuk, S. *Lecture Notes in Chemistry "Basis Sets in Computational Chemistry"*

; Springer, 2018; Chapter Adaptable Gaussian Bases for Quantum Dynamics of the Nuclei.

(14) Werther, M.; Loho Choudhury, S.; Großmann, F. Coherent State Based Solutions of the Time-Dependent Schrödinger Equation: Hierarchy of Approximations to the Variational Principle. *Int. Rev. Phys. Chem.* **2021**, *40*, 81.

(15) Zhao, Y. The Hierarchy of Davydov's Ansaetze: From Guesswork to Numerically Exact Many-Body Wavefunctions. *J. Chem. Phys* **2023**, *158*, 080901.

(16) Wyatt, R. E. *Quantum Dynamics with Trajectories: Introduction to Quantum Hydrodynamics*; Springer-Verlag, 2005.

(17) Beck, M.; Jackle, A.; Worth, G.; Meyer, H. the Multiconfiguration Time-Dependent Hartree (MCTDH) Method: A Highly Efficient Algorithm for Propagating Wavepackets. *Phys. Rep.* **2000**, *324*, 1–105.

(18) Roemer, S.; Burghardt, I. Towards a Variational Formulation of Mixed Quantum-Classical Molecular Dynamics. *Mol. Phys.* **2013**, *111*, 3618–3624.

(19) Habershon, S. Linear Dependence and Energy Conservation in Gaussian Wavepacket Basis Sets. *J. Chem. Phys.* **2012**, *136*.

(20) Martinazzo, R.; Burghardt, I. Local-In-Time Error in Variational Quantum Dynamics. *Phys. Rev. Lett.* **2020**, *124*, 150601.

(21) Burghardt, I.; Giri, K.; Worth, G. A. Multimode Quantum Dynamics Using Gaussian Wavepackets: The Gaussian-Based Multiconfiguration Time-Dependent Hartree (G-MCTDH) Method Applied to the Absorption Spectrum of Pyrazine. *J. Chem. Phys.* **2008**, *129*, 174104.

(22) Bohm, D. A Suggested Interpretation of the Quantum Theory in Terms of "hidden" Variables, I and II. *Phys. Rev.* **1952**, *85*, 166–193.

(23) Rassolov, V. A.; Garashchuk, S. Bohmian dynamics on subspaces using linearized quantum force. *J. Chem. Phys.* **2004**, *120*, 6815–6825.

(24) Sanz, A. S.; Miret-Artes, S. *A Trajectory Description of Quantum Processes. I. Fundamentals: A Bohmian Perspective*; Lecture Notes in Physics; Springer, 2012; Vol. 850.

(25) Sanz, A. S.; Miret-Artes, S. *A Trajectory Description of Quantum Processes. II. Applications: A Bohmian Perspective*; Lecture Notes in Physics; Springer, 2014; Vol. 831.

(26) Kucar, J.; Meyer, H.-D.; Cederbaum, L. Time-Dependent Rotated Hartree Approach. *Chem. Phys. Lett.* **1987**, *140*, 525–530.

(27) Grossmann, F. *Theoretical Femtosecond Physics: Atoms and Molecules in Strong Laser Fields*, 3rd ed.; Springer International Publishing AG, 2018.

(28) Sun, J.; Luo, B.; Zhao, Y. Dynamics of a One-Dimensional Holstein Polaron with the Davydov Ansätze. *Phys. Rev. B* **2010**, *82*, 014305.

(29) Zhou, N.; Chen, L.; Huang, Z.; Sun, K.; Tanimura, Y.; Zhao, Y. Fast, Accurate Simulation of Polaron Dynamics and Multidimensional Spectroscopy by Multiple Davydov Trial States. *The Journal of Physical Chemistry A* **2016**, *120*, 1562–1576, PMID: 26871592.

(30) Huang, Z.; Wang, L.; Wu, C.; Chen, L.; Grossmann, F.; Zhao, Y. Polaron Dynamics with Off-Diagonal Coupling: Beyond the Ehrenfest Approximation. *Phys. Chem. Chem. Phys.* **2017**, *19*, 1655–1668.

(31) Yuan, X.; Endo, S.; Zhao, Q.; Li, Y.; Benjamin, S. C. Theory of Variational Quantum Simulation. *Quantum* **2019**, *3*, 191.

(32) Garashchuk, S.; Rassolov, V. A. Quantum dynamics with Bohmian trajectories: Energy

conserving approximation to the quantum potential. *Chem. Phys. Lett.* **2003**, *376*, 358–363.

(33) Rassolov, V.; Garashchuk, S. Local Measure of Quantum Effects in Quantum Dynamics. *J. Phys. Chem. A* **2021**, *125*, 4653–4667.

(34) Light, J. C. *Time Dependent Quantum Molecular Dynamics: Experiments and Theory*; Plenum: New York, 1992; pp 185–199, Proceedings of NATO ARW 019/92.

(35) Kosloff, R. Time-Dependent Quantum-Mechanical Methods for Molecular Dynamics. *J. Phys. Chem.* **1988**, *92*, 2087–2100.

(36) Sherratt, P. A.; Shalashillin, D. V.; Child, M. S. Description of Multidimensional Tunnelling with the Help of Coupled Coherent States Guided by Classical Hamiltonians with Quantum Corrections. *Chem. Phys.* **2006**, *322*, 127 – 134.

(37) Dutra, M.; Wickramasinghe, S.; Garashchuk, S. Multidimensional Tunneling Dynamics Employing Quantum-Trajectory Guided Adaptable Gaussian Bases. *J. Phys. Chem. A* **2020**, *124*, 9314–9325.

(38) Großmann, F. Coupled Coherent States for Tunneling Dynamics: An Interpretative Study. *IOP Conf. Ser.* **2024**,

(39) Shalashilin, D. V.; Child, M. S. Time-Dependent Quantum Propagation in Phase Space. *J. Chem. Phys.* **2000**, *113*, 10028–10036.

TOC Graphic

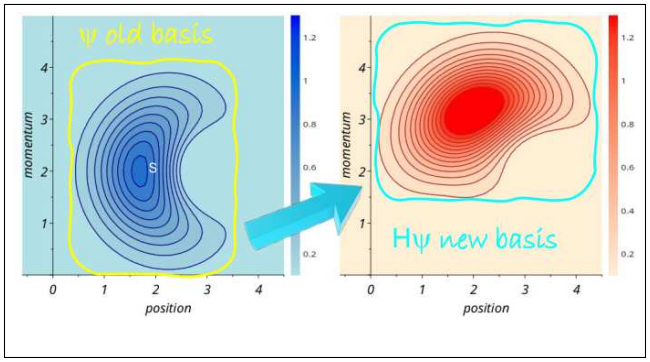
ψ old basis
momentum
position
Hψ new basis
momentum
position